Precision measurement of and search for dark matter in the transverse momentum spectra of Z bosons

by

Dylan George Hsu

Submitted to the Department of Physics
in partial fulfillment of the requirements for the degree of
Doctor of Philosophy
at the
MASSACHUSETTS INSTITUTE OF TECHNOLOGY
May 2019

Author . . . .
Department of Physics
May 1, 2019

Certified by. . . . .
Christoph Paus
Professor
Thesis Supervisor

Accepted by . . . .
John Doe
Chairman, Department Committee on Graduate Theses

Precision measurement of and search for dark matter in the transverse momentum spectra of Z bosons

by

Dylan George Hsu

Submitted to the Department of Physics
on May 1, 2019, in partial fulfillment of the
requirements for the degree of
Doctor of Philosophy

Abstract

A combined measurement of the differential Z boson production cross section in proton-proton collisions is presented. It represents the final states with charged leptons and neutrinos. This measurement furnishes a precision test of the Standard Model, constraints on the parton distribution functions of the proton, and an important component of measuring the mass of the $W^{\pm}$ boson. A study of the efficiency of lepton identification algorithms is performed which drives the precision of the measurement at lower values of transverse momentum.

In tandem, a search for new physics in events with a Z boson produced in association with large missing transverse momentum is presented. The results of this search are interpreted in the context of several dark matter models: generic spin-0 or spin-1 mediators, invisible decays of a Higgs-like boson, unparticles, and large extra spatial dimensions. A multivariate analysis was developed to enhance the sensitivity of the invisible Higgs interpretation. The theoretical uncertainty on the irreducible background from diboson processes is constrained by emulating the missing energy using pure control samples in the fully leptonic final states.

The data were collected with the Compact Muon Solenoid detector at the Large Hadron Collider and correspond to an integrated luminosity of 35.9 fb^{-1}. No significant deviations from the Standard Model are found.

Thesis Supervisor: Christoph Paus
Title: Professor

Acknowledgments

This is the acknowledgements section. You should replace this with your own acknowledgements.

Contents

List of Figures

List of Tables

Chapter 1

Reconstructing proton-proton collisions with the CMS detector

1.1 The LHC and its proton injection system

1.2 The CMS detector

The Compact Muon Solenoid (CMS) detector is a multi-purpose apparatus which operates at the LHC. It is installed about 100 metres underground close to the French village of Cessy, between Lake Geneva and the Jura mountains.

The detector requirements for CMS to meet the goals of the LHC physics programme are as follows:

- Good muon identification and momentum resolution over a wide range of momenta and angles, good dimuon mass resolution (1% at 100 GeV), and the ability to determine unambiguously the charge of muons with p < 1 TeV

- Good charged-particle momentum resolution and reconstruction efficiency in the inner tracker. Efficient triggering and offline tagging of τ's and b-jets, requiring pixel detectors close to the interaction region

- Good electromagnetic energy resolution, good diphoton and dielectron mass resolution (1% at 100 GeV), wide geometric coverage, π^0 rejection, and efficient photon and lepton isolation at high luminosities

- Good missing-transverse-energy and dijet-mass resolution, requiring hadron calorimeters with a large hermetic geometric coverage and with fine lateral segmentation

The central feature of the CMS apparatus is a superconducting solenoid of 6 m internal diameter, providing a magnetic field of 3.8 T. Within the solenoid volume are a silicon pixel and strip tracker, a lead tungstate crystal electromagnetic calorimeter (ECAL), and a brass and scintillator hadron calorimeter (HCAL), each composed of a barrel and two endcap sections. Forward calorimeters extend the pseudorapidity

coverage provided by the barrel and endcap detectors. Muons are detected in gas-ionization chambers embedded in the steel flux-return yoke outside the solenoid.

Events of interest are selected using a two-tiered trigger system [11]. The first level, composed of custom hardware processors, uses information from the calorimeters and muon detectors to select events at a rate of around 100 kHz within a time interval of less than 4 μs. The second level, known as the high-level trigger, consists of a farm of processors running a version of the full event reconstruction software optimized for fast processing, and reduces the event rate to around 1 kHz before data storage.

1.2.1 Trackers

The inner tracking system of CMS is designed to provide a precise and efficient measurement of the trajectories of charged particles emerging from the LHC collisions, as well as a precise reconstruction of secondary vertices. It surrounds the interaction point and has a length of 5.8 m and a diameter of 2.5 m. The CMS solenoid provides a homogeneous magnetic field of 4 T over the full volume of the tracker. At the LHC design luminosity of 1034 cm^{-2} s^{-1}, there are on average about 1000 particles from more than 20 overlapping proton-proton interactions traversing the tracker for each bunch crossing, i.e. every 25 ns. Therefore, a detector technology featuring high granularity and fast response is required, such that the trajectories can be identified reliably and attributed to the correct bunch crossing. However, these features imply a high power density of the on-detector electronics which in turn requires efficient cooling. This is in direct conflict with the aim of keeping to the minimum the amount of material in order to limit multiple scattering, bremsstrahlung, photon conversion and nuclear interactions. A compromise had to be found in this respect. The intense particle flux will also cause severe radiation damage to the tracking system. The main challenge in the design of the tracking system was to develop detector components able to operate in this harsh environment for an expected lifetime of 10 years. These requirements on granularity, speed and radiation hardness lead to a tracker design entirely based on silicon detector technology. The CMS tracker is composed of a pixel detector with three barrel layers at radii between 4.4 cm and 10.2 cm and a silicon strip tracker with 10 barrel detection layers extending outwards to a radius of 1.1 m. Each system is completed by endcaps which consist of 2 disks in the pixel detector and 3 plus 9 disks in the strip tracker on each side of the barrel, extending the acceptance of the tracker up to a pseudorapidity of $|\eta| < 2.5$. With about 200 m^2 of active silicon area the CMS tracker is the largest silicon tracker ever built.

1.2.2 Electromagnetic calorimeter

The electromagnetic calorimeter of CMS (ECAL) is a hermetic homogeneous calorime-ter made of 61 200 lead tungstate (PbWO$_4$) crystals mounted in the central barrel part, closed by 7 324 crys- tals in each of the two endcaps. A preshower detector is placed in front of the endcap crystals. Avalanche photodiodes (APDs) are used as photodetectors in the barrel and vacuum phototriodes (VPTs) in the endcaps. The use of high density crystals has allowed the design of a calorimeter which is fast, has
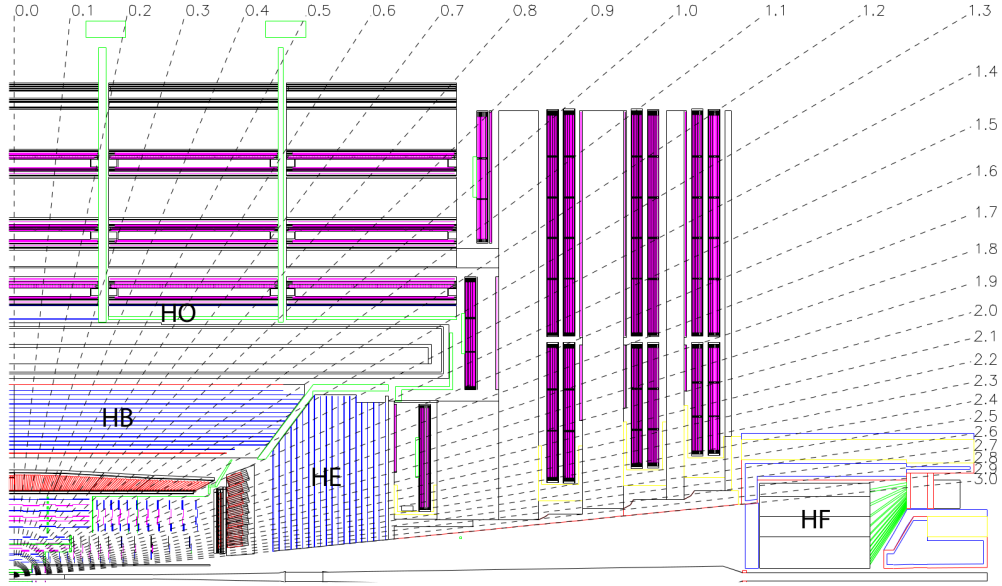
Figure 1-1: Longitudinal slice of the CMS detector showing the locations of the hadron barrel (HB), endcap (HE), outer (HO) and forward (HF) calorimeters.

fine granularity and is radiation resistant, all important characteristics in the LHC environment. One of the driving criteria in the design was the capability to detect the decay to two photons of the postulated Higgs boson. This capability is enhanced by the good energy resolution provided by a homogeneous crystal calorimeter.

1.2.3   Hadron calorimeters

The hadron calorimeters (HCALs) are particularly important for the measurement of hadron jets and neutrinos or exotic particles resulting in apparent missing transverse energy [1]. Figure 1-1 shows the longitudinal view of the CMS detector. The dashed lines are at fixed η values. The hadron calorimeter barrel and endcaps sit behind the tracker and the electromagnetic calorimeter as seen from the interaction point. The hadron calorimeter barrel is radially restricted between the outer extent of the electromagnetic calorimeter (R = 1.77 m) and the inner extent of the magnet coil (R = 2.95 m). This constrains the total amount of material which can be put in to absorb the hadronic shower. Therefore, an outer hadron calorimeter or tail catcher is placed outside the solenoid complementing the barrel calorimeter. Beyond $|\eta| = 3$, the forward hadron calorimeters placed at 11.2 m from the interaction point extend the pseudorapidity coverage down to $|\eta| = 5.2$ using a Cherenkov-based, radiation-hard technology. The HCAL subsystems are described briefly below, with more detailed information on the geometry and readout being available in [1].

HCAL barrel

The HCAL barrel (HB) is a sampling calorimeter and covers the pseudorapidity range $|\eta| < 1.3$. It consists of 36 identical azimuthal wedges which form two half-barrels. The wedges are constructed out of flat brass absorber plates which are parallel to the beam axis. Each wedge is segmented into four azimuthal angle (ϕ) sectors. The innermost and outermost plates are made of stainless steel for structural strength.

The absorber consists of a front steel plate 40 mm thick, followed by eight 50.5 mm thick brass plates, six 56.5 mm thick brass plates, and a 75 mm thick steel back plate. The last layer is thicker to correct for late developing showers which could leak out the back. The total absorber thickness at 90° is 5.82 interaction lengths (λ_I). The HB effective thickness increases with polar angle (θ) as $1/\sin\theta$, resulting in 10.6 λ_I at $|\eta| = 1.3$.

The HB baseline active material is 3.7 mm thick Kuraray SCSN81 plastic scintillator, chosen for its long-term stability and moderate radiation hardness. The first layer of scintillator is located in front of the steel support plate, and is made of 9 mm thick Bicron BC408. Its purpose is to sample hadronic showers developing in the inert material between the ECAL barrel and the HCAL barrel. The plastic scintillator is divided into 16 η sectors, resulting in a segmentation of $(\Delta\eta, \Delta\phi) = (0.087, 0.087)$.

HCAL endcaps

The hadron calorimeter endcaps (HE) cover the rapidity range $1.3 < |\eta| < 3$. It is designed for high radiation tolerance, in order to survive 10 MRad after 10 years of operation. The total length of the endcap calorimeter, after the ECAL and HCAL endcaps, is about 10 interaction lengths.

The absorber is made of C26000 cartridge brass, due to its mechanical properties, its high number of interaction lengths, and its relatively low cost. Furthermore, it may sit in the 4 T axial magnetic field. The absorber is assembled in a staggered geometry which minimizes the cracks between HB and HE and contains no projective dead material.

The scintillators are of trapezoidal shape and there are 18 layers of them in total. The first layer are made of 9 mm thick Bicron BC408. All the rest are made of 3.7 mm thick SCSN81. The scintillation light is read out via wavelength shifting fibers. The granularity of the calorimeters is $(\Delta\eta, \Delta\phi) = (0.087, 0.087)$ for $|\eta| < 1.6$ and $(\Delta\eta, \Delta\phi) = (0.170, 0.170)$ for $|\eta| \geq 1.6$.

HCAL outer

The combined stopping power of the ECAL and HCAL barrels does not provide adequate stopping power in the central region $|\eta| < 1.3$. This is problematic for the missing energy resolution. To further measure and contain these showers, the hadron calorimeter is extended outside the solenoid with a tail catcher called the HO. Only 40 mm of space in the radial direction is available, 24 mm of which is used for aluminum honeycomb support structures.

The scintillator plates of the HO are made of 10 mm thick Bicron BC408. There are 5 rings in η, each of those rings having 12 identical ϕ sectors, and each of those sectors having 6 azimuthal slices. The sizes and positions of the tiles in HO are supposed to roughly map the layers of HB to make towers of granularity $(\Delta\eta, \Delta\phi) = (0.087, 0.087)$.

The magnetic solenoid coil is used as an additional absorber equal to $1.4/\sin\theta$ interaction lengths. Outside the vacuum tank, the magnetic field is returned through an iron yoke roughly 20 mm thick, with 5 rings corresponding to the scintillator plates. The central ring has scintillators both inside and outside of the iron yoke ring. The others have scintillators only outside their yoke rings. All told, the total depth of the calorimeter system is extended to a minimum of $11.8\,\lambda_I$ except at the barrel-endcap boundary region.

HCAL forward

The forward calorimeter, or HF, exists in an extremely hostile environment. At $|\eta| = 5$ we expect to have delivered 10 MGy after 10 years of operation. The active material is fused-silica core, polymer hard-cladded quartz fibers, which have sufficient radiation hardness. These fibers measure $600 \pm 10\,\mu$m in diameter for the fused-silica core, $630^{+5}_{-10}\,\mu$m with the polymer hard-cladding, and $800 \pm 30\,\mu$m with the protective acrylate buffer.

The geometry consists of a steel absorber structure composed of 5 mm thick grooved plates. Fibers are inserted in these grooves. The detector is functionally subdivided into two longitudinal segments. Half of the fibers run over the full depth of the absorber (165 cm $\approx 10\,\lambda_I$) while the other half starts at a depth of 22 cm from the front of the detector. These two sets of fibers are read out separately. This arrangement makes it possible to distinguish showers generated by electrons and photons, which deposit a large fraction of their energy in the first 22 cm, from those generated by hadrons, which produce nearly equal signals in both calorimeter segments on average. The absorber has grooves which make a square grid separated by 5.0 ± 0.1 mm center-to-center, with long and short fibers alternating in the grooves.

This calorimeter is mostly sensitive to the electromagnetic component of hadronic showers. Only light that hits the core-cladding interface at an angle larger than the critical angle ($71°$) contributes to the calorimeter signal in the form of Cherenkov light. After the quoted 10 MGy dose has accumulated over the HF lifetime, the optical transmission of the fibers is reduced just by a factor of 2.

1.2.4   Muon systems

1.3   Object reconstruction

1.3.1   Electrons

Electrons in the CMS detector are reconstructed through association of a track from the silicon detector with a cluster of energy in the ECAL. Electron tracks are formed

from initial seeds likely to correspond to initial electron trajectories, which are then used to build tracks by collecting hits in the silicon tracker using the combinatorial Kalman filter procedure. Next, a track fitting procedure is undertaken using a Gaussian Sum Filter (GSF), in which the energy loss in each tracker layer is approximated by a mixture of Gaussian distributions. Meanwhile, the electron energy has been collected in several crystals of the ECAL. These depositions undergo two steps of clustering. The first step finds clusters from crystal arrays of 5×1 in $\eta \times \phi$ for the ECAL barrel, and 5×5 crystals for the ECAL endcaps. The second step forms a supercluster (SC) comprising the energy of constituent clusters. The supercluster position and energy, along with the GSF track, reconstruct the electron in the detector.[9] The reconstruction procedure is also informed by the Particle-Flow algorithm, described later in Section ???.

The final electron momentum is found using a multivariate regression tuned on simulation to give better energy resolution. A residual energy scale correction is applied to the reconstructed electrons based on time, electron η, and shower shape variables such that the Z mass peak resolution is enhanced. In addition, a smearing is applied to simulation such that the energy resolution in data and simulation match.

The isolation of the lepton candidates is computed from the flux of particle flow candidates found within a cone of $\Delta R = 0.4$ built around the lepton direction [7]. The flux of particles is computed independently for the charged hadrons, neutral hadrons and photon candidates. The contribution from neutral hadron candidates is corrected for the influence of PU by using the *effective area* approach. The average energy density per area due to PU (ρ) is multiplied with an effective area (A_{eff}) and subtracted from the isolation sum. A_{eff} is chosen in such a way that the isolation is independent of the number of pileup interactions. The relative electron isolation sum is defined as:

$$I_{\text{rel}}^e = \frac{1}{p_{\text{T}}} \left[I_{\text{ch}} + \max(I_{\text{nh}} + I_{\text{g}} - A_{\text{eff}} \cdot \rho, 0) \right] \tag{1.1}$$

1.3.2 Muons

Muon tracks are reconstructed in the CMS detector in both the silicon tracker and the muon spectrometer, resulting respectively in tracker tracks and standalone-muon tracks. Subsequently, these tracks inform two reconstruction approaches:

1. *Global Muon reconstruction (outside-in):* starting from a standalone muon in the muon system, a matching tracker track is found and a *global-muon track* is fitted combining hits from the tracker track and standalone-muon track. At large transverse momenta ($p_{\text{T}} \gtrsim 200$ GeV/c), the global-muon fit can improve the momentum resolution compared to the tracker-only fit.

2. *Tracker Muon reconstruction (inside-out):* in this approach, all tracker tracks with $p_{\text{T}} > 0.5$ GeV/c and $p > 2.5$ GeV/c are considered as possible muon candidates and are extrapolated to the muon system, taking into account the expected energy loss and the uncertainty due to multiple scattering. If at least

one muon segment (i.e. a short track stub made of DT or CSC hits) matches the extrapolated track, the corresponding tracker track qualifies as a *tracker-muon track*. The extrapolated track and the segment are considered to be matched if the distance between them in local x is less than 3 cm or if the value of the pull for local x is less than 4. At low momentum (roughly $p < 5$ GeV/c) this approach is more efficient than the global muon reconstruction, since it requires only a single muon segment in the muon system, whereas global muon reconstruction is designed to have high efficiency for muons penetrating through more than one muon station.

The majority of muons from collisions (with sufficient momentum) are reconstructed either as a Global Muon or a Tracker Muon, or very often as both. A third, rare case is excluded from this note, where both approaches fail and only a *standalone-muon track* is found [8].

For the muon isolation, in the same manner as for electrons, a cone of $\Delta R = 0.4$ is built to compute the flux of particle flow candidates, the "delta-beta" correction is applied to correct for pileup contamination. This correction is achieved by subtracting half the sum of the p_T of the charged particles in the cone of interest but with particles not originating from the primary vertex. The muon isolation is therefore defined as:

$$I_{\text{rel}}^{\mu} = \frac{1}{p_T} \left[I_{\text{ch}} + \max(I_{\text{nh}} + I_{\text{g}} - 0.5 \cdot I_{\text{chPU}}, 0) \right] \tag{1.2}$$

The factor 0.5 corresponds to a approximate average of neutral to charged particles and has been measured in jets in [7].

1.3.3 Jets

Jets are reconstructed from all the particle flow candidates using the anti-k_{t} clustering algorithm [4] with a distance parameter of 0.4, as implemented in the FASTJET package [5, 3]. The reconstruction may be seeded using all reconstructed particle flow candidates after having removed the charged hadron candidates which are not associated to the primary vertex of the event (charge hadron subtracted AK4PFchs). The energy of the reconstructed jets is corrected in 3 steps: L1FastJet (for pileup/underlying event subtraction), L2 (for relative corrections), and L3 (for absolute scale corrections). For data, an extra residual correction is included in the absolute scale correction, derived by the JetMET working group within the CMS collaboration.

An extra correction is applied for the simulated jets in order to reproduce the measured jet energy resolution. For each jet the transverse momentum is smeared using using the transverse momentum of the generator level matched jet and the measured Data/MC resolution ratio. The correction transformation is given by:

$$p_T \rightarrow \max\left[0, p_T^{\text{gen}} + c \cdot (p_T - p_T^{\text{gen}})\right] \tag{1.3}$$

in which $c = \sigma_{\text{data}}/\sigma_{\text{MC}}$ are the data-to-MC resolution scale factors.

We consider for analysis all jets with $p_T >$20 GeV and $|\eta| < 5$ passing a set of loose identification requirements given in Table 1.1. Jets that are within $\Delta R < 0.4$

of one of the identified leptons are disregarded, this is referred to as "jet cleaning". The number of jets is used as a selection variable. Here, we define it as how many of these nominal jets have $p_T > 30$ GeV and $|\eta| < 2.4$.

Quantity	Requirement
Neutral Hadron Fraction	< 0.99
Neutral EM Fraction	< 0.99
Number of Constituents	> 1
Charged Hadron Fraction	> 0
Charged Multiplicity	> 0
Charged EM Fraction	< 0.99

Table 1.1: Loose jet identification criteria for jets having $|\eta| < 2.4$.

For the purpose of rejecting events involving top quark production, jets originating from b quark fragmentation (b jets) are identified by "b tagging." The b tagging technique employed is based on the "combined secondary vertex" CSVv2 algorithm [6]. The algorithm is calibrated to provide, on average, 80% efficiency for tagging jets originating from b quarks, and 10% probability of light-flavor jet misidentification.

1.3.4 Photons

Photon candidates are reconstructed from energy deposits in the ECAL using algorithms that constrain the clusters to the size and shape expected from a photon [10] . The identification of the candidates is based on shower-shape and isolation variables, and depends on whether the energy deposit was in the ECAL Barrel or Endcap. For isolated photons, scalar sums of the p_T of PF candidates within a cone of $\Delta R < 0.3$ around the photon candidate are required to be below the bounds defined. Only the PF candidates that do not overlap with the EM shower of the candidate photon are included in the isolation sums. The photon candidates used in this analysis are required to have a minimum p_T of 15 GeV and to be within $|\eta| < 2.5$ passing the loose identification criteria given in Table 1.2.

Quantity	ECAL Barrel Req.	ECAL Endcap Req.
Full 5x5 $\sigma_{i\eta i\eta}$	< 0.0103	< 0.0301
H/E	< 0.0597	< 0.0481
charged hadron isolation	< 1.295	< 1.011
neutral hadron isolation	$< 10.92 + (0.0148 \text{ GeV}^{-1})p_T$ $+(1.7 \times 10^{-5} \text{ GeV}^{-2})p_T{}^2$	$< 5.931 + (0.0163 \text{ GeV}^{-1})p_T$ $+(1.4 \times 10^{-5} \text{ GeV}^{-2})p_T{}^2$
photon isolation	$< 3.630 + (0.0047 \text{ GeV}^{-1})p_T$	$< 6.641 + (0.0034 \text{ GeV}^{-1})p_T$
Conversion safe electron veto	Yes	Yes

Table 1.2: Loose photon identification criteria.

1.3.5 Particle-flow reconstruction

The particle-flow (PF) event reconstruction algorithm [12] is used. It is designed to leverage information from all CMS detector components to reconstruct and identify individual particles, namely: electrons, muons, photons, and charged and neutral hadrons. The reconstructed vertex with the largest value of summed physics-object p_T^2 is taken to be the primary proton-proton interaction vertex. The physics objects are the track-jets, clustered using the jet finding algorithm [4, 5] with the tracks assigned to the vertex as inputs, and the associated missing transverse momentum, taken as the negative vector sum of the p_T of those jets.

1.3.6 Missing transverse energy

The missing transverse momentum vector, $\vec{p}_T^{\mathrm{miss}}$, is defined as the projection of the negative vector sum of the momenta of all reconstructed PF candidates in an event onto the plane perpendicular to the beams. Its magnitude is referred to as E_T^{miss}. Several event-level filters are applied to discard events with anomalous E_T^{miss} arising from specific well-understood issues with the detector components or event reconstruction [2]. Jet energy corrections are propagated to the missing transverse momentum by adjusting the momentum vector of the PF candidate constituents of each reconstructed jet.

Chapter 2

Data samples

2.1 Experimental data

This analysis uses a sample of pp collisions collected in 2016 with the CMS experiment at the LHC at $\sqrt{s}$ = 13 TeV. Five primary datasets are used to ensure a very high trigger efficiency: MuEG, DoubleMuon, DoubleElectron, SingleMuon, and SingleElectron. All data are analyzed using the

Cert_271036-284044_13TeV_23Sep2016ReReco_Collisions16_JSON.txt

file in order to select the good luminosity sections. The total integrated luminosity with the associated uncertainty is 35.9 $\pm$ 0.9 fb^{-1}.

2.2 Simulated samples

Several Monte Carlo (MC) event generators are used to simulate the signal and background processes. For all processes, the detector response is simulated using a detailed description of the CMS detector, based on the GEANT4 package [?], and event reconstruction is performed with the same algorithms as used for data. The simulated samples include additional interactions per bunch crossing (pileup). The simulated events are weighted so that the pileup distribution matches the data, with an average pileup of about 25 interactions per bunch crossing.

2.2.1 Standard Model processes

Resonant Z boson background processes (WZ, ZZ, tribosons, etc.) are estimated using Monte Carlo (MC) samples. Nonresonant background processes ($t\bar{t}$, tW, WW, $Z/\gamma^* \to \tau^+\tau^-$, etc.) are estimated using eμ data events.

The WZ and ZZ processes, via $q\bar{q}$ annihilation, are generated at next-to-leading-order (NLO) with POWHEG2.0 [?, ?, ?, ?]. The gg $\to$ ZZ process is simulated with MCFM [?]. The Zγ, t$\bar{t}$Z, WWZ, WZZ, and ZZZ processes are generated with MADGRAPH5_AMC@NLO [?]. The signal samples are simulated using MADGRAPH5_AMC@NLO at next-to-leading-order (NLO), MADGRAPH5 at leading-order (LO), and POWHEG at NLO. The default MC generator is MADGRAPH5_AMC@NLO.

The PYTHIA8 [?, ?] package is used for parton showering, hadronization, and the underlying event simulation, with tune CUETP8M1. The NNPDF 3.0 [?] set is used as the default set of parton distribution functions (PDFs). The processed dataset names and cross sections for the Standard Model processes considered in the analysis are shown in Table 2.1. Simulated datasets from the RunIISummer16MiniAODv2 campaign are used.

2.2.2 Dark matter hypotheses

Samples of simulated DM particle events in the simplified model are generated using MADGRAPH5_AMC@NLO 2.2.2 [?] at leading order (LO) and matched to PYTHIA 8.205 [?] using tune CUETP8M1 for parton showering and hadronization [?, ?]. The factorization and renormalization scales are set to the geometric mean of $\sqrt{p_T^2 + m^2}$ for all final-state particles [?, ?], where p_T and m are the transverse momentum and mass of each particle.

For the simplified model of DM production, couplings are chosen according to the recommendations in Ref. [?]. The coupling g_χ is set to one. For g_q, values of 1.0 and 0.25 are considered. The width of the mediator is assumed to be determined exclusively by the contributions from the couplings to quarks and the DM particle χ. Under this assumption, the width ranges 1–5% (30–50%) of the mediator mass for $g_q = 0.25$ ($g_q = 1.00$). The signal simulation samples with $g_q = 1.0$ are processed using the detector simulation described below. Signal predictions for $g_q = 0.25$ are obtained by applying event weights based on the E_T^{miss} distribution at the generator level to the fully simulated samples with $g_q = 1.0$. This procedure takes into account the nontrivial dependence of the mediator width on the coupling choice [?]. The exact dependence of the width on the model parameters is reported in [?].

Events for the ADD extra-dimension scenario are generated at LO using an EFT implementation in PYTHIA 8 [?, ?]. Event samples are produced for $M_D = 1, 2$ and 3 TeV, each with $n = 2, 3, 4, 5, 6, 7$. The signal is truncated for $\hat{s} > M_D^2$ in order to ensure the validity of the EFT.

The events for the unparticle model are generated at LO with PYTHIA 8 [?, ?] assuming a cutoff scale $\Lambda_U = 15$ TeV, using tune CUETP8M1 for parton showering and hadronization. We evaluate other values of Λ_U by rescaling the cross sections as needed. The parameter Λ_U acts solely as a scaling factor for the cross section and does not influence the kinematic distributions of unparticle production [?].

The ZH production modes via q$\bar{q}$ annihilation and gluon-gluon fusion are modeled the same way as for the WZ and ZZ processes.

A comparison of kinematic spectra for various signal models is shown in Figs. ?? and ??.

2.3 Corrections to the simulated samples

2.3.1 Pileup reweighting

2.3.2 Lepton selection efficiencies

2.3.3 Lepton momentum scale and resolution

Table 2.1: Processed dataset names and cross sections for the Standard Model processes considered in the analysis. The processes are grouped in the following way: Resonant Diboson, Triboson, Nonresonant, and Drell-Yan.

Process	Simulated sample name	Cross section [pb]
$WZ \to 3\ell\nu$	WZTo3LNu_TuneCUETP8M1_13TeV-powheg-pythia8	4.42965×1.109
$WZ \to 2\ell 2q$	WZTo2L2Q_13TeV_amcatnloFXFX_madspin_pythia8	5.595×1.109
$ZZ \to 4\ell$	ZZTo4L_13TeV_powheg_pythia8	1.256
$gg \to ZZ \to 4\mu$	GluGluToContinToZZTo4mu_13TeV_MCFM701_pythia8	0.001586×2.3
$gg \to ZZ \to 4e$	GluGluToContinToZZTo4e_13TeV_MCFM701_pythia8	0.001586×2.3
$gg \to ZZ \to 4\tau$	GluGluToContinToZZTo4tau_13TeV_MCFM701_pythia8	0.001586×2.3
$gg \to ZZ \to 2\mu 2e$	GluGluToContinToZZTo2e2mu_13TeV_MCFM701_pythia8	0.003194×2.3
$gg \to ZZ \to 2\mu 2\tau$	GluGluToContinToZZTo2mu2tau_13TeV_MCFM701_pythia8	0.003194×2.3
$gg \to ZZ \to 2e2\tau$	GluGluToContinToZZTo2e2tau_13TeV_MCFM701_pythia8	0.003194×2.3
$gg \to ZZ \to 2\mu 2\nu$	GluGluToContinToZZTo2mu2nu_13TeV_MCFM701_pythia8	0.001720×2.3
$gg \to ZZ \to 2e2\nu$	GluGluToContinToZZTo2e2nu_13TeV_MCFM701_pythia8	0.001720×2.3
$ZZ \to 2\ell 2\nu$	ZZTo2L2Nu_13TeV_powheg_pythia8	0.564
$ZZ \to 2\ell 2q$	ZZTo2L2Q_13TeV_amcatnloFXFX_madspin_pythia8	3.220
$Z + \gamma$	ZGTo2LG_TuneCUETP8M1_13TeV-amcatnloFXFX-pythia8	117.864
WZZ	WZZ_TuneCUETP8M1_13TeV-amcatnlo-pythia8	0.05565
WWZ	WWZ_TuneCUETP8M1_13TeV-amcatnlo-pythia8	0.16510
ZZZ	ZZZ_TuneCUETP8M1_13TeV-amcatnlo-pythia8	0.01398
$Z \to \tau\tau \to e\mu$	DYJetsToTauTau_ForcedMuEleDecay_M-50_TuneCUETP8M1_13TeV-amcatnlo-pythia8	$1921.8 * (0.1741 + 0.1783)^2$
$qq \to WW \to 2\ell 2\nu$	WWTo2L2Nu_13TeV-powheg	$(118.7\text{-}3.974) \times 0.1086 \times 0.1086 \times 9$
$gg \to WW \to 2\ell 2\nu$	GluGluWWTo2L2Nu_MCFM_13TeV	$(3.974 \times 0.1086 \times 0.1086 \times 9 \times 1.4$
$\mathrm{t\bar{t}}Z(\ell\ell + \nu\nu)$	TTZToLLNuNu_M-10_TuneCUETP8M1_13TeV-amcatnlo-pythia8	0.2529
$\mathrm{t\bar{t}}Z(qq)$	TTZToLLNuNu_M-10_TuneCUETP8M1_13TeV-amcatnlo-pythia8	0.5297
$\mathrm{t\bar{t}}W(\ell\nu)$	TTWJetsToLNu_TuneCUETP8M1_13TeV-amcatnloFXFX-madspin-pythia8	0.2043
$\mathrm{t\bar{t}}W(qq)$	TTWJetsToQQ_TuneCUETP8M1_13TeV-amcatnloFXFX-madspin-pythia8	0.4062
$\mathrm{t\bar{t}} \to 2\ell 2\nu 2b$	TTTo2L2Nu_13TeV-powheg	$831.76 \times 0.1086 \times 0.1086 \times 0.1086 \times 9$
tW	ST_tW_top_5f_inclusiveDecays_13TeV-powheg-pythia8	35.6
tW	ST_tW_antitop_5f_inclusiveDecays_13TeV-powheg-pythia8	35.6
$Z/\gamma^* \to \ell^+\ell^-$	DYJetsToLL_M-50_TuneCUETP8M1_13TeV-amcatnloFXFX-pythia8	2008×3
	DYJetsToLL_M-10to50_TuneCUETP8M1_13TeV-amcatnloFXFX-pythia8	$2008.4 \times 3 \times 3.78$
	DYJetsToLL_M-50_TuneCUETP8M1_13TeV-madgraphMLM	2008×3
	ZToLL_NNPDF30_13TeV-powheg_M_50_120	1975×2
	DYJetsToLL_Pt-50To100_TuneCUETP8M1_13TeV-amcatnloFXFX-pythia8	375
	DYJetsToLL_Pt-100To250_TuneCUETP8M1_13TeV-amcatnloFXFX-pythia8	86.5
	DYJetsToLL_Pt-250To400_TuneCUETP8M1_13TeV-amcatnloFXFX-pythia8	3.32
	DYJetsToLL_Pt-400To650_TuneCUETP8M1_13TeV-amcatnloFXFX-pythia8	0.449
	DYJetsToLL_Pt-650ToInf_TuneCUETP8M1_13TeV-amcatnloFXFX-pythia8	0.0422

Appendix A

Tables

Table A.1: Armadillos

Armadillos	are
our	friends

Appendix B

Figures

Figure B-1: Armadillo slaying lawyer.

Figure B-2: Armadillo eradicating national debt.

Bibliography

[1] *Technical proposal*. LHC Tech. Proposal. CERN, Geneva, 1994. Cover title : CMS, the Compact Muon Solenoid : technical proposal.

[2] Performance of missing energy reconstruction in 13 TeV pp collision data using the CMS detector. Technical Report CMS-PAS-JME-16-004, CERN, Geneva, 2016.

[3] M. Cacciari and G. P. Salam. Dispelling the N^3 myth for the k_t jet-finder. *Phys. Lett. B*, 641:57, 2006.

[4] M. Cacciari, G. P. Salam, and G. Soyez. The Anti-k(t) jet clustering algorithm. *JHEP*, 04:063, 2008.

[5] Matteo Cacciari, Gavin P. Salam, and Gregory Soyez. FastJet user manual. *Eur. Phys. J. C*, 72:1896, 2012.

[6] Serguei Chatrchyan et al. Identification of b-quark jets with the CMS experiment. 2012.

[7] CMS Collaboration. Commissioning of the particle-flow reconstruction in minimum-bias and jet events from pp collisions at 7 TeV. *CMS Physics Analysis Summary*, CMS-PAS-PFT-10-002, 2010.

[8] CMS Collaboration. Performance of muon identification in 2010 data. *CMS Physics Analysis Summary*, CMS-PAS-MUO-10-004, 2010.

[9] CMS Collaboration. Performance of electron reconstruction and selection with the cms detector in proton-proton collisions at sqrt(s) = 8 tev. *JINST 10 (2015) P06005*, page 6, 2015.

[10] Vardan Khachatryan et al. Performance of photon reconstruction and identification with the CMS detector in proton-proton collisions at $\sqrt{s} = 8$ TeV. *JINST*, 10:P08010, 2015.

[11] Vardan Khachatryan et al. The CMS trigger system. *JINST*, 12:P01020, 2017.

[12] Albert M Sirunyan et al. Particle-flow reconstruction and global event description with the CMS detector. *JINST*, 12:P10003, 2017.